STRUCTURAL BIOLOGY

# Structure of the nuclear exosome captured on a maturing preribosome

Jan Michael Schuller,[1]* Sebastian Falk,[1]* Lisa Fromm,[2] Ed Hurt,[2]† Elena Conti[1]†

**The RNA exosome complex processes and degrades a wide range of transcripts, including ribosomal RNAs (rRNAs). We used cryo–electron microscopy to visualize the yeast nuclear exosome holocomplex captured on a precursor large ribosomal subunit (pre-60S) during 7S-to-5.8S rRNA processing. The cofactors of the nuclear exosome are sandwiched between the ribonuclease core complex (Exo-10) and the remodeled "foot" structure of the pre-60S particle, which harbors the 5.8S rRNA precursor. The exosome-associated helicase Mtr4 recognizes the preribosomal substrate by docking to specific sites on the 25S rRNA, captures the 3′ extension of the 5.8S rRNA, and channels it toward Exo-10. The structure elucidates how the exosome forms a structural and functional unit together with its massive pre-60S substrate to process rRNA during ribosome maturation.**

The eukaryotic RNA exosome is a conserved 3′-5′ degradation machinery that functions in the turnover, surveillance, and processing of coding and noncoding RNAs, in both the nucleus and the cytoplasm (*1*, *2*). The processing of ribosomal RNA (rRNA) precursors is a prominent function of the nuclear exosome (*3*). In yeast, ribosome biogenesis starts with the synthesis of a polycistronic transcript, from which the 18*S*, 5.8*S*, and 25*S* rRNAs are generated by a series of processing reactions (*4*, *5*). One of the most complex steps in rRNA biogenesis is the degradation of the internal transcribed spacer 2 (ITS2), an intervening sequence located between the 5.8*S* and 25*S* rRNAs that is almost completely removed before the pre-60*S* ribosomal particle is exported to the cytoplasm (*4*) (fig. S1). ITS2 removal requires the action of the exosome and is indeed the pathway that led to the discovery of this complex in *Saccharomyces cerevisiae* (*6*).

The yeast exosome contains a core complex of 10 proteins (Exo-10), which include a single processive 3′-5′ exoribonuclease (Rrp44) and nine catalytically inactive subunits (Exo-9) (*1*, *2*, *7*). RNA substrates reach the ribonuclease via an internal channel that traverses the entire core complex and can accommodate up to 30 nucleotides (*8*, *9*). In the nucleus, Exo-10 functions with four conserved cofactors: the distributive 3′-5′ exoribonuclease Rrp6, its binding partner Rrp47, the small protein Mpp6, and the 3′-5′ RNA helicase Mtr4 (*1*, *3*). Rrp6-Rrp47 and Mpp6 stably associate with the exosome core and together contribute to transiently recruit Mtr4 (*10*–*13*). In turn, Mtr4 is transiently recruited by ribosome biogenesis factors to catalyze the removal of rRNA spacer sequences (*14*).

The removal of ITS2 from the pre-60*S* particle starts with cleavage reactions that generate the 5′ end of the mature 25*S* rRNA but leave behind a 5.8*S* rRNA precursor with a long 3′ end extension (7*S*) (fig. S1) (*4*, *5*). Subsequent trimming of the 7*S* pre-rRNA by the exosome occurs through the sequential action of the two nuclear exosome ribonucleases (*15*, *16*). Rrp44 first shortens the 3′ end of the 7*S* pre-rRNA to a 5.8*S* rRNA form extended by 30 nucleotides (5.8*S*+30); Rrp6 then takes over this intermediate and shortens the extension further (fig. S1) (*15*, *16*). Similar pre-rRNA intermediates have been observed in mammalian cells, suggesting that the mechanism of exosome-mediated 7*S*-to-5.8*S* rRNA processing is conserved from yeast to human (*17*).

The individual steps in ribosomal biogenesis not only entail the progressive shortening of rRNA precursors but also correlate with discrete preribosomal particles that differ in the composition of ribosomal proteins and transiently associated biogenesis factors (*4*). Recent cryo–electron microscopy (cryo-EM) reconstructions have revealed the architecture of pre-60*S* particles containing the 7*S* pre-rRNA, showing how ribosomal biogenesis factors assemble around part of ITS2 and form the so-called "foot" structure of the particle (*18*). The finding that one of these biogenesis factors, Nop53, recruits the Mtr4 helicase (*14*) has paved the way for visualizing the structure of a nuclear exosome as it processes the 5.8*S* rRNA in a pre-60*S* ribosome particle.

We recently reconstituted the yeast 7*S* pre-rRNA processing reaction in vitro using endogenous 7*S*-containing pre-60*S* particles (purified by tagging Nop53) together with an active recombinant nuclear exosome holo-complex (Exo-10–Rrp6–Rrp47–Mpp6–Mtr4, referred to as Exo-14n) (*19*). For the structural analysis, we stalled the exosome on the pre-60*S* using an Exo-14n complex with a catalytically inactive Rrp6 (*12*), which accumulates unprocessed 5.8*S*+30 pre-rRNA (*19*) (fig. S1). Single-particle cryo-EM analysis of the purified pre-60*S*–Exo-14n complex yielded EM density maps ranging between 3.9- and 4.6-Å resolution (figs. S2 to S5 and table S1), of sufficient quality to unambiguously fit all the known atomic models (see materials and methods) (fig. S6). The resulting pseudo-atomic model reveals the architecture of the entire pre-60*S*–Exo-14n assembly intermediate, stalled on a 5.8*S*+30 pre-rRNA (5.8*S*+30 particle) (Fig. 1).

The inner core of the in vitro–processed pre-60*S* particle has a very similar overall structure as compared with the 7*S* pre-rRNA containing pre-60*S* particles (7*S* particles) previously isolated from yeast via either Nog2 (*18*) or Arx1 (*20*). However, there are pronounced differences. First, the L1 stalk, a flexible structural element formed within domain V of the 25*S* rRNA, has swiveled about 30° into a half-inward conformation, with its tip contacting the immature unrotated 5*S* ribonucleoprotein (RNP) (fig. S7). Second, the foot

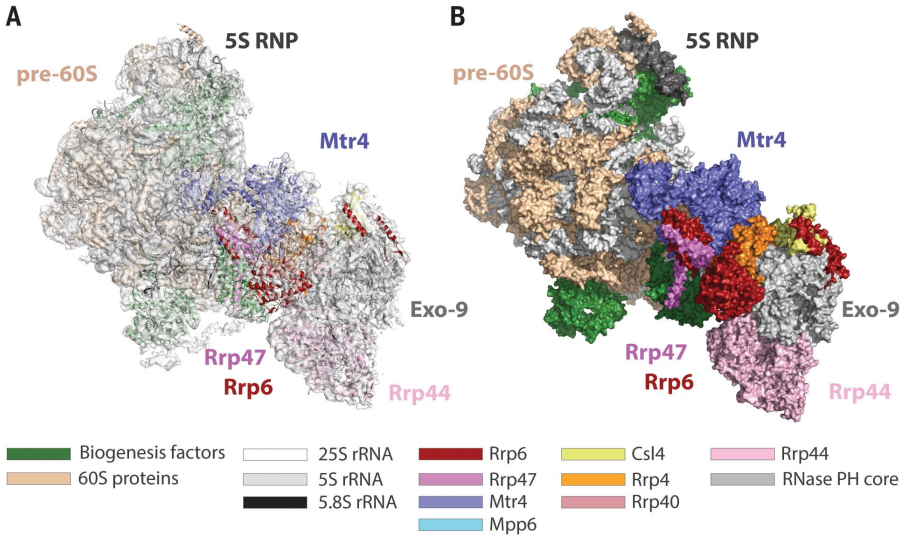


**Fig. 1. Overall structure of the yeast pre-60S–Exo-14n complex.** (**A**) Cryo-EM density and (**B**) surface representation of the pre-60S–Exo-14n structure fitted with known atomic structures. The color-coding scheme for the different proteins and RNAs is indicated at the bottom. The 5.8S rRNA is embedded within the complex and not visible in the surface representation.

[1]Department of Structural Cell Biology, Max Planck Institute (MPI) for Biochemistry, Munich, Germany. [2]Biochemistry Centre, University of Heidelberg, Heidelberg, Germany.
*These authors contributed equally to this work.
†Corresponding author. Email: conti@biochem.mpg.de (E.C.); ed.hurt@bzh.uni-heidelberg.de (E.H.)

structure at the bottom of the pre-60*S* particle has been almost completely remodeled. In the earlier 7*S* particles, the foot is formed by five ribosome biogenesis factors, which coat the structured part at the 3′ extension of the 5.8*S* rRNA (*18*) (fig. S8, A and B). In the 5.8*S*+30 particle, only one of these assembly factors (Nop7) has remained bound in the same conformation (Fig. 1 and fig. S8, A and B). No ordered density is visible for Nop53, which had been used as the bait for pre-60*S* purification, suggesting that it may be flexibly attached after remodeling or dissociated during the EM sample preparation (fig. S8C). Furthermore, the convoluted structure at the 3′ extension of the 5.8*S* rRNA has been unfolded and trimmed and is now embedded in a single-stranded conformation within the exosome channel (see below). The physical space previously occupied by the ITS2 RNP in the 7*S* particle is now occupied by the bulky Mtr4 and the other exosome cofactors (Fig. 2 and fig. S8B).

The Mtr4 helicase provides the main connection between the pre-60*S* and Exo-10. Mtr4 contains a catalytic core (a DExH-type helicase region formed by two RecA and a helical bundle domain) and a regulatory "arch" (*21*, *22*) [formed by a helical "stalk" and a KOW (Kyrpides, Ouzounis, and Woese) domain]. In our cryo-EM structure, Mtr4 binds the 25*S* rRNA via a bidentate interaction mediated both by the arch and by the DExH core (Fig. 2A and fig. S6B). Within the arch, the KOW domain contacts domain I of the 25*S* rRNA (at helices 15 and 16) (Fig. 2A) using structural elements that had been previously shown to bind double-stranded RNA in nuclear magnetic resonance mapping experiments (*23*). In this orientation, the Nop53-binding site on the KOW domain is solvent accessible (*14*, *23*) (fig. S8D), suggesting that the arch can in principle bind both Nop53 and the 25*S* rRNA during the early stages of recruitment to the 7*S* particle (*23*). In general, these KOW-rRNA interactions, which we observe in our map, rationalize previous functional data that the arch of Mtr4 is required for rRNA processing in vivo (*22*).

The DExH core of Mtr4 contacts domain V of the 25*S* rRNA (Fig. 2A). The helical bundle domain approaches a eukaryotic-specific element of the 25*S* rRNA (helix 79 in expansion segment ES31), whereas the RecA2 domain contacts an adjacent surface at the base of the L1 stalk (helix 76, near ribosomal protein L8). Altogether, these interactions push the L1 stalk upward, possibly causing long-range effects to the tip of the L1 stalk and stabilizing it in its half-inward conformation. Importantly, some of the contacts between Mtr4 and domain V of the 25*S* rRNA would only be feasible after the foot structure has been remodeled and the biogenesis factor Rlp7 been removed. It is thus possible to envisage how Mtr4 could signal the state of ITS2 processing to the L1 stalk, which in turn could trigger the next ribosome biogenesis steps (e.g., the recruitment of Rix1-Rea1 and rotation of the 5*S* RNP) (*24*).

The DExH-binding and KOW-binding regions in the 25*S* rRNA are separated by about 90 Å (Fig. 2A). To span this distance, the arch domain of Mtr4 moves from the bent conformation captured in previous crystal structures (*21*, *22*) to a more extended state. Interestingly, a similar conformational change has been observed with

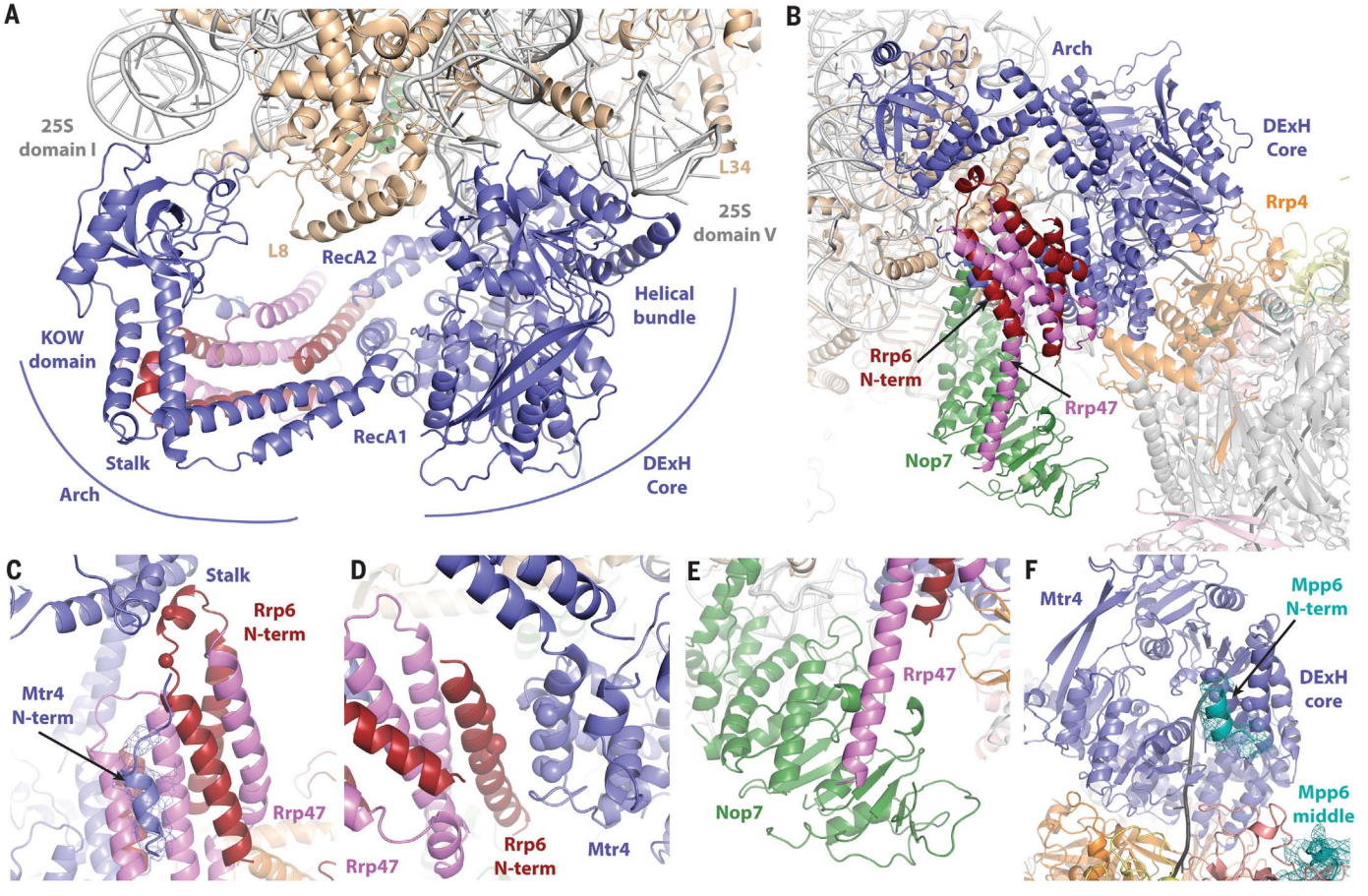


**Fig. 2. The nuclear cofactors of the RNA exosome.** (**A**) Mtr4 (blue) with the pre-60S particle (25S rRNA gray, ribosomal proteins wheat). (**B**) $Rrp6_N$-$Rrp47_N$ (red and pink) with Mtr4 and the biogenesis factor Nop7 (green). (**C**) $Rrp6_N$-$Rrp47_N$ concave surface with the N-terminal region of Mtr4 (*30*), shown with the corresponding cryo-EM density. Red spheres represent the position of residues mutated in a previous study [Rrp6 $Asp^{27}$ and $Phe^{30}$ (*30*)]. (**D**) $Rrp6_N$-$Rrp47_N$ convex surface with the DExH core of Mtr4. Spheres identify positions of conserved negatively charged residues of Rrp6 and conserved positively charged residues of Mtr4. (**E**) C-terminal helix of $Rrp47_N$ with Nop7. (**F**) Bottom surface of the Mtr4 DExH core with additional cryo-EM density (attributed to N terminus of Mpp6, cyan). Blue spheres represent the position of residues mutated in Mtr4 that abolish binding to Mpp6.

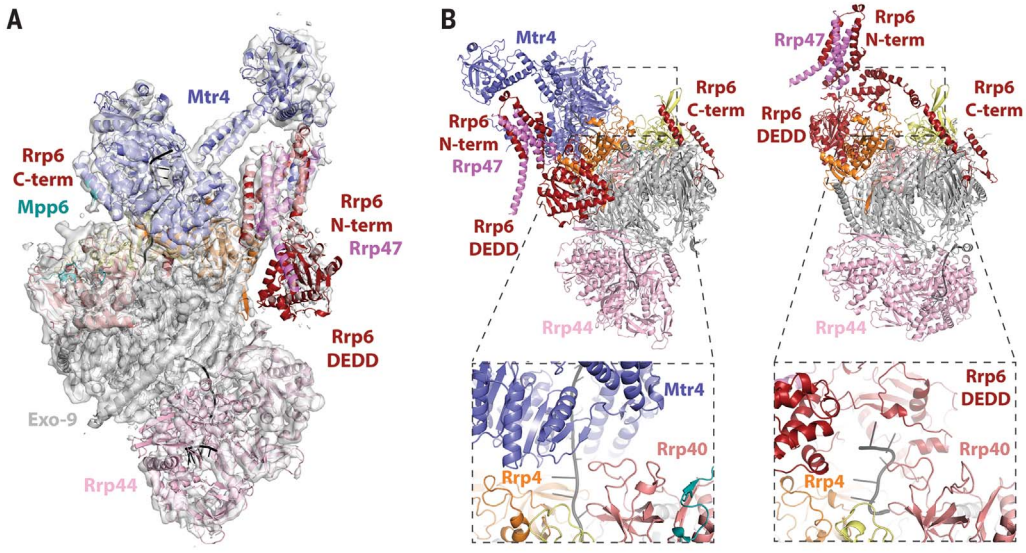


**Fig. 3. Open and closed conformations of nuclear exosome complexes.** (**A**) View of the Exo-14n structure from the complex with the pre-60S particle (with cryo-EM density) showing the edge-on position of Mtr4 on top of Exo-9. (**B**) (Left) Exo-14n complex rotated ~180° around a vertical axis with respect to (A) showing Rrp6 in an open conformation. (Right) Exo-12n crystal structure (*16*) in the same orientation, showing Rrp6 in a closed conformation. The zoom-in views at the bottom show how Mtr4 and Rrp6 dock on the same surface of the exosome subunit Rrp4 (orange).

the homologous cytoplasmic helicase Ski2 upon binding to the 80*S* ribosome (*25*). In our cryo-EM structure, the extended conformation of the Mtr4 arch appears to be stabilized by the $Rrp6_N$-$Rrp47_N$ module, a tightly intertwined heterodimer formed by the N-terminal domains of the two proteins (*26*) (Fig. 2B). Fitting the characteristic crescent-shaped structure of $Rrp6_N$-$Rrp47_N$ was unambiguous in the EM density (fig. S6C). Confirming the interpretation, the EM reconstruction showed additional density on the concave surface of the $Rrp6_N$-$Rrp47_N$ crescent (Fig. 2C), consistent with the binding of the Mtr4 N-terminal region (*26*). On the convex surface of $Rrp6_N$-$Rrp47_N$, a helix of Rrp6 lined by negatively charged residues approaches the helical bundle domain of Mtr4 at a conserved positively charged surface (Fig. 2D and fig. S6D). At the tip of $Rrp6_N$-$Rrp47_N$, a conserved loop of Rrp6 reaches the stalk helices of the Mtr4 arch (Fig. 2C and fig. S2C). This observation rationalizes previous in vivo data that mutations of conserved residues in this loop result in a 5.8*S* rRNA processing defect in yeast (*26*). Finally, a characteristic feature of $Rrp6_N$-$Rrp47_N$ is the presence of a long α helix in $Rrp47_N$ (*26*). This helix protrudes by more than 20 Å from the crescent and attaches to the pre-60*S* particle by binding to the only remaining biogenesis factor at the remnant foot structure, Nop7 (Fig. 2E and fig. S6E).

Besides visualizing how Mtr4 docks to the pre-60*S* particle, the EM reconstruction reveals how it binds to the exosome complex. The Exo-9 core is formed by an upper ring of three "cap" proteins (Rrp4, Rrp40, and Csl4) and a lower ring of six ribonuclease (RNase) PH-like proteins (*1*, *7*). The helicase core of Mtr4 is positioned edge-on at the top of Exo-9 (Fig. 3A). The helical bundle and RecA1 domains of Mtr4 bind the cap protein Rrp4 (Fig. 3B, left panel) and in particular approach a conserved loop of Rrp4 that is known to be essential in vivo (*27*). Previous structural studies have shown that the same surface of Rrp4 binds the ribonuclease domain of Rrp6 (*12*, *13*, *28*) (Fig. 3B, right panel). This "closed" conformation of Rrp6 appears to be the resting position in exosome complexes lacking Mtr4 (*12*). In the pre-60*S*–Exo-14n complex, Mtr4 binding onto Rrp4 appears to have displaced the Rrp6 ribonuclease module into an "open" conformation, on the side of Exo-9. In this open conformation, the Rrp6 ribonuclease module is rather flexible, with only a portion [the helicase and RNaseD C-terminal (HRDC) domain] accounted for in the EM density (Fig. 3A), reminiscent of (although not identical to) another flexible open conformation observed in previous crystallographic studies (*12*). Essentially, the only part of Rrp6 that remains unchanged in all structures determined to date is the C-terminal exosome-binding domain (Fig. 3B and fig. S6F) (*8*, *12*, *13*, *28*).

The incorporation of yeast Mtr4 into Exo-14n also requires Mpp6 (*10*, *26*). Structural studies have shown how the middle domain of Mpp6 binds the cap protein Rrp40 at the top of Exo-9 (*10*, *11*). From biochemical studies, the N-terminal domain of Mpp6 is expected to contribute to binding Mtr4 (*10*) and channeling RNA through it (*11*), but the mechanisms have remained unclear. In the reconstruction, we noticed a density feature on the helicase core of Mtr4 that would be unexplained by the fitting of available crystal structures and that would correspond dimension-wise to a helix (Fig. 2F and fig. S6G). This structural feature docks onto conserved hydrophobic residues at the bottom of the DExH core ($Ile^{443}$ and $Ile^{489}$) and points toward the middle domain of Mpp6 (Fig. 2F and fig. S9). We reasoned that this density might correspond to the conserved N-terminal domain of Mpp6. Indeed, isothermal titration calorimetry experiments showed that Mpp6 residues 1 to 67 bind the DExH core of Mtr4 with a dissociation constant $K_d$ of ~25 μM (fig. S9A). The interaction was impaired when using the I443R/N446R or I489R/E493R mutants of Mtr4 or when deleting the conserved N-terminal segment of Mpp6 (residues 1 to 26) in pull-down experiments (fig. S9C and S9D).

After fitting the Exo-14n proteins, we identified and traced the 3′ extension of the 5.8*S* rRNA in a prominent density that emerges from the pre-60*S* particle and extends into Exo-14n (Fig. 4). After the final nucleotide of the 5.8*S* rRNA (nucleotide 158), the ribonucleotide chain continues and enters into the DExH core of Mtr4. Here, the density follows the same path that had been observed in the crystal structure of RNA-bound Mtr4 (*21*) (Fig. 4). Upon exiting the helicase, the density weakens as it crosses the solvent region between the edge-on base of Mtr4 and the top of Exo-9. Well-defined density starts again as the RNA reaches the cap proteins and enters the internal channel of the exosome core. RNA traverses Exo-9, as previously observed in the crystal structure of Exo-10-$Rrp6_C$ (*8*). The major difference is that the RNA chain ends in the PIN domain of Rrp44 rather than in the exoribonuclease domain. Such a path from Exo-9 to the PIN domain had already been suggested in previous studies (*29*, *30*). In the context of our reconstruction, the most plausible interpretation is that we captured a situation/state whereby the 3′ extension of 5.8*S* has been trimmed to ~30 nucleotides but cannot be handed over to Rrp6 for further trimming (because Rrp6 exoribonuclease is inactivated) and hence is re-captured in the exosome channel. Considering that Exo-14n has a footprint of 40 nucleotides in RNase protection assays (*11*), the path toward the PIN domain might simply reflect the best fit for a 30-nucleotide extension in a "resting" state of Exo-14n, when Mtr4 is in an edge-on position on top of Exo-9. The Mtr4-channeling conformation of the nuclear exosome that we observed in our reconstruction is likely to be relevant not only for the pre-60*S* substrate. Indeed, RNase protection assays of Exo-14n bound to a generic single-stranded RNA recapitulate the predictions from the cryo-EM reconstruction, namely that the arch domain of Mtr4 is required for RNA channeling (fig. S10).

This study shows how the nuclear RNA exosome remodels the pre-60*S* particle, both in

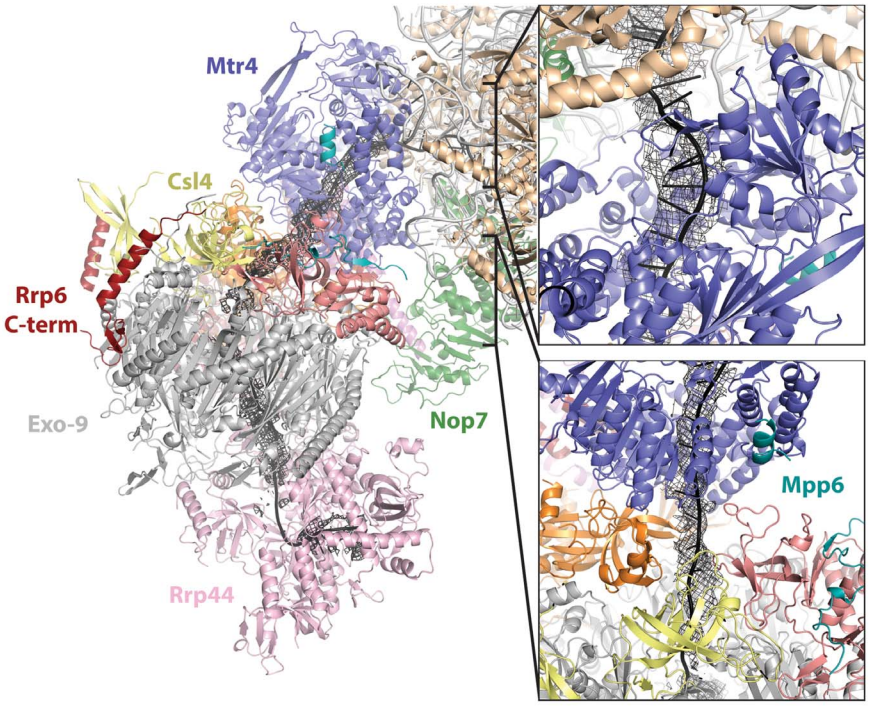


**Fig. 4. The path of the 3′ extension of the 5.8*S* rRNA from the pre-60*S* particle to the exosome.** (Left) Close-up view of the cryo-EM structure, with the density corresponding to the 3′ extension of the 5.8*S* rRNA as a black mesh. (Right) Zoom-in panels showing the RNA as it exits the pre-60*S* particle and enters Mtr4 (top) and as it exits Mtr4 and enters Exo-9 (bottom).

composition and structure, thereby signaling the status of ITS2 processing to the ribosome core. The exosome complex itself is remodeled upon binding to the preribosome: Its cofactors undergo dramatic conformational changes as they rearrange to channel the 3′ extension of the 5.8*S* rRNA through the Mtr4 helicase and into the degradative chamber. Trapping the exosome in action on a pre-60*S* particle has given an unprecedented snapshot of how this RNA shredding machine works on such a complex substrate. Although the macromolecular complexes that degrade RNAs and synthesize proteins have so far been studied individually, this work sets the stage to elucidating how different machineries in eukaryotic gene expression are physically coupled and coordinated.

## REFERENCES AND NOTES


1. J. C. Zinder, C. D. Lima, *Genes Dev.* **31**, 88–100 (2017).
2. A. Chlebowski, M. Lubas, T. H. Jensen, A. Dziembowski, *Biochim. Biophys. Acta* **1829**, 552–560 (2013).
3. C. Kilchert, S. Wittmann, L. Vasiljeva, *Nat. Rev. Mol. Cell Biol.* **17**, 227–239 (2016).
4. J. L. Woolford Jr., S. J. Baserga, *Genetics* **195**, 643–681 (2013).
5. E. Thomson, S. Ferreira-Cerca, E. Hurt, *J. Cell Sci.* **126**, 4815–4821 (2013).
6. P. Mitchell, E. Petfalski, A. Shevchenko, M. Mann, D. Tollervey, *Cell* **91**, 457–466 (1997).
7. D. L. Makino, F. Halbach, E. Conti, *Nat. Rev. Mol. Cell Biol.* **14**, 654–660 (2013).
8. D. L. Makino, M. Baumgärtner, E. Conti, *Nature* **495**, 70–75 (2013).
9. F. Bonneau, J. Basquin, J. Ebert, E. Lorentzen, E. Conti, *Cell* **139**, 547–559 (2009).
10. E. V. Wasmuth, J. C. Zinder, D. Zattas, M. Das, C. D. Lima, *eLife* **6**, e29062 (2017).
11. S. Falk, F. Bonneau, J. Ebert, A. Kögel, E. Conti, *Cell Reports* **20**, 2279–2286 (2017).
12. D. L. Makino *et al.*, *Nature* **524**, 54–58 (2015).
13. E. V. Wasmuth, K. Januszyk, C. D. Lima, *Nature* **511**, 435–439 (2014).
14. M. Thoms *et al.*, *Cell* **162**, 1029–1038 (2015).
15. C. Allmang *et al.*, *EMBO J.* **18**, 5399–5410 (1999).
16. M. W. Briggs, K. T. D. Burkard, J. S. Butler, *J. Biol. Chem.* **273**, 13255–13263 (1998).
17. L. Tafforeau *et al.*, *Mol. Cell* **51**, 539–551 (2013).
18. S. Wu *et al.*, *Nature* **534**, 133–137 (2016).
19. L. Fromm *et al.*, *Nat. Commun.* **8**, 1787 (2017).
20. B. Bradatsch *et al.*, *Nat. Struct. Mol. Biol.* **19**, 1234–1241 (2012).
21. J. R. Weir, F. Bonneau, J. Hentschel, E. Conti, *Proc. Natl. Acad. Sci. U.S.A.* **107**, 12139–12144 (2010).
22. R. N. Jackson *et al.*, *EMBO J.* **29**, 2205–2216 (2010).
23. S. Falk *et al.*, *RNA* **23**, 1780–1787 (2017).
24. B. Tutuncuoglu, J. Jakovljevic, S. Wu, N. Gao, J. L. Woolford Jr., *RNA* **22**, 1386–1399 (2016).
25. C. Schmidt *et al.*, *Science* **354**, 1431–1433 (2016).
26. B. Schuch *et al.*, *EMBO J.* **33**, 2829–2846 (2014).
27. H. Malet *et al.*, *EMBO Rep.* **11**, 936–942 (2010).
28. J. C. Zinder, E. V. Wasmuth, C. D. Lima, *Mol. Cell* **64**, 734–745 (2016).
29. K. Drażkowska *et al.*, *Nucleic Acids Res.* **41**, 3845–3858 (2013).
30. E. V. Wasmuth, C. D. Lima, *Mol. Cell* **48**, 133–144 (2012).


## ACKNOWLEDGMENTS

We would like to thank I. Schäfer, R. Prabu, and F. Beck for discussions on EM; P. Reichelt for help with yeast growths; D. Fleming for initial negative-stain images; F. Bonneau for the assay in fig. S10; E. Stegmann for technical support in protein purification; P. Cramer and T. Schulz for giving us access to yeast fermentation; M. Strauss for giving superb assistance and training to access the microscopes of the MPIB cryo-EM Facility; and members of our groups for comments and discussions. **Funding:** This study was supported by the Max Planck Gesellschaft E.C., the European Commission (ERC Advanced Investigator Grants EXORICO to E.C. and Glowsome to E.H.), the Deutsche Forschungsgemeinschaft (DFG SFB646, SFB1035, GRK1721, and CIPSM to E.C. and HU363/10-5 and HU363/12-1 to E.H.), and the Louis Jeantet Foundation (to E.C.). **Author contributions:** E.C. and E.H. initiated the project; L.F., S.F., and J.M.S. identified initial biochemical conditions; J.M.S. and S.F. carried out cryo-EM sample preparation; J.M.S. collected cryo-EM data and performed image processing; J.M.S. built the structure with help from S.F.; S.F. carried out recombinant in vitro assays; and J.M.S., S.F., L.F., E.C., and E.H. analyzed the structure and wrote the paper. **Competing interests:** The authors declare no competing financial interests. **Data and materials availability:** The cryo-EM density maps are deposited in the Electron Microscopy Data Bank under accession numbers EMD-4301 and EMD-4302. The atomic model is deposited in the Protein Data Bank (PDB) under accession numbers 6FSZ and 6FT6. All other data are available in the manuscript or the supplementary materials.

## SUPPLEMENTARY MATERIALS

www.sciencemag.org/content/360/6385/219/suppl/DC1
Materials and Methods
Figs. S1 to S10
Table S1
References (*31*–*36*)

21 November 2017; accepted 22 February 2018
Published online 8 March 2018
10.1126/science.aar5428

# Structure of the nuclear exosome captured on a maturing preribosome

Jan Michael Schuller, Sebastian Falk, Lisa Fromm, Ed Hurt and Elena Conti

*Science* **360** (6385), 219-222.
DOI: 10.1126/science.aar5428originally published online March 8, 2018

**The RNA exosome captured in action**

The RNA exosome, a major RNA degradation machine, processes ribosomal RNA (rRNA) precursors and is directly coupled to the protein synthesis machine, the ribosome. Using cryo–electron microscopy, Schuller *et al.* investigated the structure of the precursor large ribosomal subunit from yeast with unprocessed rRNA in complex with the RNA exosome. The structure captures a snapshot of two molecular machines transiently interacting and explains how the RNA exosome acts on an authentic physiological substrate and remodels the large subunit during ribosome maturation.

*Science*, this issue p. 219